Nanoscale magnetic resonance imaging

C. L. Degen[a], M. Poggio[a,b], H. J. Mamin[a], C. T. Rettner[a], and D. Rugar[a,1]

[a]IBM Research Division, Almaden Research Center, 650 Harry Road, San Jose, CA 95120; and [b]Center for Probing the Nanoscale, Stanford University, 476 Lomita Mall, Stanford, CA 94305

Communicated by Stuart S. P. Parkin, IBM Almaden Research Center, San Jose, CA, December 1, 2008 (received for review August 21, 2008)

We have combined ultrasensitive magnetic resonance force microscopy (MRFM) with 3D image reconstruction to achieve magnetic resonance imaging (MRI) with resolution <10 nm. The image reconstruction converts measured magnetic force data into a 3D map of nuclear spin density, taking advantage of the unique characteristics of the "resonant slice" that is projected outward from a nanoscale magnetic tip. The basic principles are demonstrated by imaging the ^{1}H spin density within individual tobacco mosaic virus particles sitting on a nanometer-thick layer of adsorbed hydrocarbons. This result, which represents a 100 million-fold improvement in volume resolution over conventional MRI, demonstrates the potential of MRFM as a tool for 3D, elementally selective imaging on the nanometer scale.

MRFM | MRI | nuclear magnetic resonance | molecular structure imaging

Magnetic resonance imaging (MRI) is well-known in medicine and in the neurosciences as a powerful tool for acquiring 3D morphological and functional information with resolution in the millimeter-to-submillimeter range (1, 2). Unfortunately, despite considerable effort, attempts to push the spatial resolution of conventional MRI into the realm of high-resolution microscopy have been stymied by fundamental limitations, especially detection sensitivity (3, 4). Consequently, the highest resolution MRI microscopes today remain limited to voxel volumes >40 μm^3 (5–8). The central issue is that MRI is based on the manipulation and detection of nuclear magnetism, and nuclear magnetism is a relatively weak physical effect. It appears that conventional coil-based inductive detection techniques simply cannot provide adequate signal-to-noise ratio for detecting voxel volumes below the micrometer size. This sensitivity constraint is unfortunate because MRI has much to offer the world of microscopy with its unique contrast modalities, its elemental selectivity, and its avoidance of radiation damage.

Despite the many challenges, there is strong motivation to extend MRI to finer resolution, especially if the nanometer scale can be reached. At the nanometer scale, one might hope to directly and nondestructively image the 3D structure of individual macromolecules and molecular complexes (9). Such a powerful molecular imaging capability could be of particular interest to structural biologists trying to unravel the structure and interactions of proteins, especially for those proteins that cannot be crystallized for X-ray analysis, or are too large for conventional NMR spectroscopy. Nanoscale MRI, with its capacity for true 3D, subsurface imaging, its potential for generating contrast by selective isotopic labeling and its nondestructive nature, would be a welcome complement to the characteristics of electron microscopy. The key to pushing MRI to the nanoscale is detection sensitivity.

Recently, a significant breakthrough in magnetic resonance detection sensitivity has been achieved by using magnetic resonance force microscopy (MRFM) (9–13), resulting in single spin detection for electrons (14) and substantial progress in nuclear spin detection (15–24). Despite the great progress in nuclear spin MRFM, only one previous nanoscale imaging experiment has been demonstrated, and it was limited to 90-nm resolution in 2 dimensions for ^{19}F nuclei in an inorganic test sample (25). Here, we report that MRFM can perform 3D MRI of ^{1}H nuclear spins (protons) in a biological specimen [tobacco mosaic virus (TMV) particles] with a spatial resolution down to 4 nm. This capability is enabled by several key technical advances, including the generation of magnetic field gradients as high as 4 million Tesla (T) per meter, detailed understanding of the MRFM point-spread function, and application of an image-reconstruction technique capable of converting magnetic force measurements into a 3D map of proton density.

Principles

MRFM is based on mechanical measurement of ultrasmall (attonewton) magnetic forces between nuclear spins in a sample and a nearby magnetic tip. Basic elements of our MRFM apparatus are shown in Fig. 1. The test sample consists of individual TMV particles that are deposited onto the flat end of an ultrasensitive silicon cantilever. The end of the cantilever is positioned close to a 200-nm-diameter magnetic tip that produces a strong and very inhomogeneous magnetic field. The magnetic tip sits on a copper "microwire" that serves to efficiently generate a radiofrequency (rf) magnetic field that excites NMR (26). Frequency modulation of the rf field induces periodic inversions of the ^{1}H spins in the sample, resulting in a periodic force that drives the mechanical resonance of the cantilever. Monitoring the cantilever oscillation amplitude while mechanically scanning the magnetic tip with respect to the sample in 3 dimensions provides data that allow the reconstruction of the ^{1}H density. The imaging is performed in vacuum and at low temperature (T = 300 mK).

The TMV particles are deposited onto the cantilever in solution and then air dried. (See supporting information (SI) *Appendix* for preparation details.) As shown in Fig. 1*B*, the sample consists of both whole virus and smaller fragments. The TMV particles, which have a rod-like geometry with diameter of 18 nm and lengths up to 300 nm (27, 28), were chosen as test objects because they are physically robust and have a size suitable for evaluating our imaging resolution. They also serve to demonstrate that MRFM is capable of imaging native biological specimens. Approximately 95% of the virus mass consists of protein, resulting in a ^{1}H density estimated to be $\rho = 4 \times 10^{28}$ spins per m^3. In the future, rapid freezing techniques, such as used in cryoelectron microscopy, could be used to better preserve the structural integrity of fully hydrated biological samples (29, 30).

NMR will only occur if the ^{1}H spins in the sample are at the correct field for satisfying the Larmor resonance condition: $B_0(\mathbf{r}) = \omega_0/\gamma \equiv B_{\text{res}}$, where ω_0 is the rf field frequency, and $\gamma = 2\pi \times 42.57$ MHz/T is the proton gyromagnetic ratio. The field $B_0(\mathbf{r}) \equiv |B_{\text{ext}}\hat{\mathbf{z}} + \mathbf{B}_{\text{tip}}(\mathbf{r})|$ is supplied by the combination of the field from an external superconducting magnet, B_{ext}, and the field from the magnetic tip, $\mathbf{B}_{\text{tip}}(\mathbf{r})$, where $\mathbf{r}$ is the position with respect to the tip apex. For an rf center frequency of $\omega_0 = 2\pi \times$

Author contributions: C.L.D., M.P., H.J.M., and D.R. designed research; C.L.D., M.P., H.J.M., and D.R. performed research; C.T.R. contributed new reagents/analytic tools; C.L.D., M.P., H.J.M., and D.R. analyzed data; and C.L.D., M.P., and D.R. wrote the paper.

The authors declare no conflict of interest.

[1]To whom correspondence should be addressed. E-mail: rugar@almaden.ibm.com.

This article contains supporting information online at www.pnas.org/cgi/content/full/0812068106/DCSupplemental.

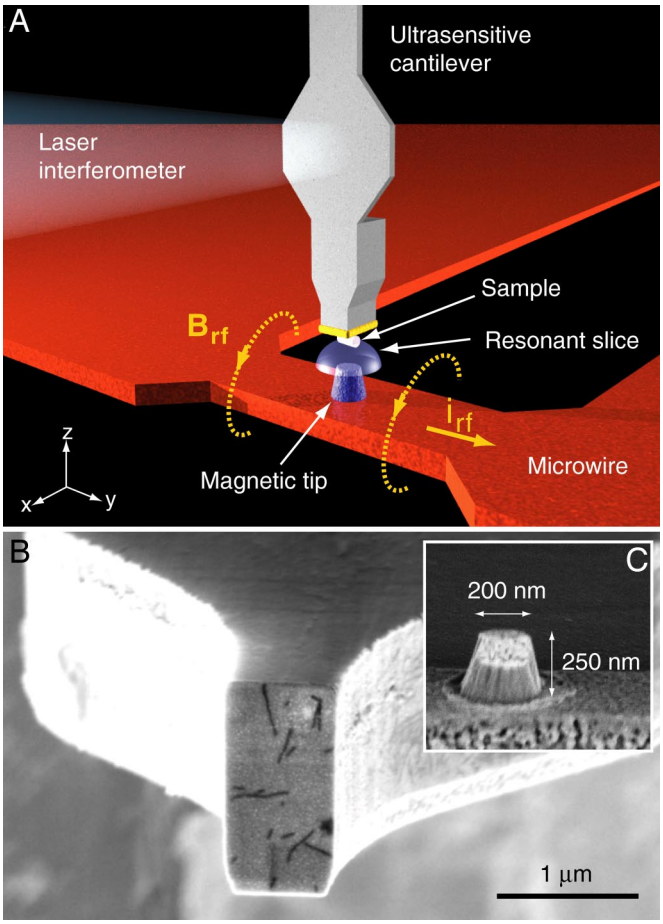

Fig. 1. Configuration of MRFM apparatus. (*A*) Tobacco mosaic virus particles, attached to the end of an ultrasensitive silicon cantilever, are positioned close to a magnetic tip. A rf current i_{rf} passing through a copper microwire generates an alternating magnetic field B_{rf} that induces magnetic resonance in the ^{1}H spins of the virus particles. The resonant slice represents those points in space where the field from the magnetic tip (plus an external field) matches the condition for magnetic resonance. Three-dimensional scanning of the tip with respect to the cantilever, followed by image reconstruction is used to generate a 3D image of the spin density in the virus sample. (*B*) Scanning electron micrograph of the end of the cantilever. Individual tobacco mosaic virus particles are visible as long, dark rods on the 0.8-μm × 1.3-μm-sized sample platform. (*C*) Detail of the magnetic tip.

114.8 MHz, the resonance condition is met for $B_0(\mathbf{r}) = 2.697$ T. Because the field from the magnetic tip is a strong function of position, the resonance is confined to a thin, approximately hemispherical "resonant slice" that extends outward from the tip (Figs. 1*A* and 2). The field gradient at the resonant slice can exceed 4×10^6 T/m at a distance of 25 nm from the tip, resulting in a slice thickness that is as thin as a few nanometers. The rf field is frequency modulated with a peak deviation of $\Delta\omega_{rf,peak} = 2\pi \times$ 600 kHz in order to drive adiabatic inversions of the protons. The periodicity of the spin inversion is chosen to match the mechanical resonance of the cantilever (≈2.9 kHz). In the presence of the field gradient from the magnetic tip, the spin inversions generate a small oscillating force, typically on the order of 10 aN-rms, that excites a slight (subangstrom) vibration of the cantilever. The vibration is detected by a fiber-optic interferometer and lock-in amplifier.

The spin signal originates from the naturally occurring $\sqrt{N}$ statistical polarization of the spin ensemble ("spin noise"), where N is the number of ^{1}H spins in the measurement volume (19, 23, 31–33). Using the statistical polarization is advantageous because its root-mean-square amplitude exceeds the mean Boltzmann polarization for nanoscale volumes of spins (23). Statistical polarization is also convenient because there is no need to wait a spin-lattice relaxation time T_1 for the spins to polarize. Because the statistical polarization can be either positive or negative, we detect the signal power (i.e., the spin signal variance), which is proportional to the density of ^{1}H in the sample. We use the term "spin signal" to mean the estimated variance of the force that has spin origin, with units of aN^2. See ref. 23 and *SI Appendix* for additional details of the signal acquisition.

Three-dimensional imaging of the sample requires 2 steps: data collection and image reconstruction. First, the spin signal is measured as the magnetic tip is mechanically scanned with respect to the sample in a 3D raster pattern, yielding a map of the spin signal as a function of tip position. Because of the extended geometry of the resonant slice, however, a spatial scan does not directly produce a map of the proton distribution in the sample. Instead, each data point in the scan contains spin signal contributions from a variety of depths and lateral positions. Specifically, the map $\xi(\mathbf{r}_s)$ of the signal as a function of tip scan position $\mathbf{r}_s$ is related to the proton distribution $\rho(\mathbf{r})$ by the convolution integral

$$\xi(\mathbf{r}_s) = \int_{\substack{\text{sample}\\\text{volume}}} d^3\mathbf{r}\, K(\mathbf{r}_s - \mathbf{r})\rho(\mathbf{r}), \qquad [1]$$

where $K(\mathbf{r})$ is the 3D point spread function (PSF) associated with the resonant slice. $K(\mathbf{r})$ is defined as the mean spin signal generated by a randomly polarized spin in the sample at a position $\mathbf{r}$ with respect to the magnetic tip.

The amplitude of the MRFM point-spread function is set by 2 main factors: one that determines the effectiveness of the spin inversions and confines the response to the near vicinity of the resonant slice and one that reflects the strength of the lateral field gradient at the position of the spin. As discussed in the *SI Appendix*, we find that the PSF can be approximated by

$$K(\mathbf{r}) = \begin{cases} A\mu^2[G(\mathbf{r})]^2\left[1 - \left(\dfrac{\Delta B_0(\mathbf{r})}{\Delta\omega_{rf,peak}/\gamma}\right)^2\right] & \text{for} |\Delta B_0(\mathbf{r})| \le \Delta\omega_{rf,peak}/\gamma \\ 0 & \text{for} |\Delta B_0(\mathbf{r})| > \Delta\omega_{rf,peak}/\gamma \end{cases} \qquad [2]$$

Here, $G(\mathbf{r}) \equiv \partial B_{tip,z}/\partial x$ is the lateral field gradient from the tip, $\Delta B_0(\mathbf{r}) \equiv B_0(\mathbf{r}) - \omega_0/\gamma$ is the off-resonance condition, and $\Delta\omega_{rf,peak}/\gamma \approx 14$ mT is the peak FM modulation converted to magnetic field units. The proportionality constant A depends on details of the experiment, such as the correlation time of the spin inversions and the bandwidth of the detection. $G(\mathbf{r})$ and $B_0(\mathbf{r})$ are key components of $K(\mathbf{r})$, and both require detailed knowledge of the field produced by the magnetic tip. As discussed in *SI Appendix*, we calculate $\mathbf{B}_{tip}(\mathbf{r})$ using a magnetostatic model of the tip and then tune the parameters of the model (for example, tip magnetization and geometry) to be consistent with the measured scan data. Based on Eq. **2** and our best estimates of the magnetic tip parameters, we obtain the PSF shown in Fig. 2. At a distance of 24 nm, where the peak gradient is $G = 4.2$ mT/nm, we find the shell thickness (full width at half maximum) to be as thin as $\sqrt{2}\Delta\omega_{rf,peak}/\gamma G = 4.8$ nm.

To recover the real-space proton distribution $\rho(\mathbf{r})$ from the 3D scan data $\xi(\mathbf{r}_s)$, the effect of the PSF must be deconvolved. We use an iterative Landweber algorithm that starts with an initial estimate for the spin density of the object, $\rho_0(\mathbf{r})$ and then

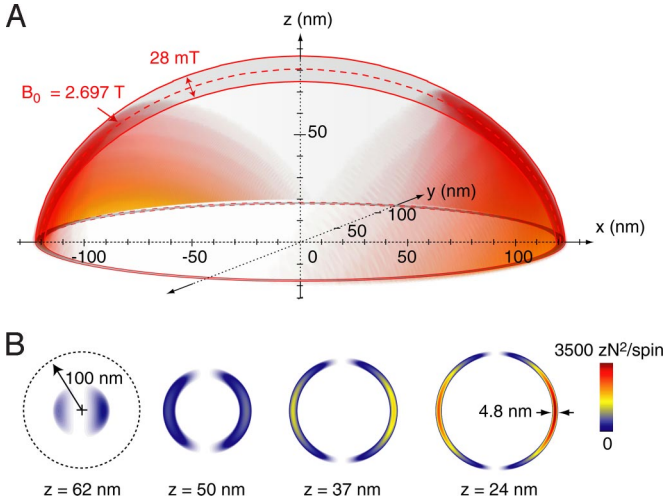

Fig. 2. Details of the resonant slice and associated point spread function (PSF). (*A*) Three-dimensional representation corresponding to the conditions $B_{res} = \omega_0/\gamma = 2.697$ T and $B_{ext} = 2.482$ T. The center of the tip apex is assumed to be at the origin of the coordinate system. The resonant slice is the hemispherical "shell" outlined in red, representing the region of space for which $B_0(\mathbf{r})$ lies within $B_{res} \pm \Delta\omega_{rf,peak}/\gamma$ (here 2.697 ± 0.014 T). Regions to the left and right of the tip (shaded red) contribute most to the signal because this is where the lateral gradient $G(\mathbf{r})$ is largest. (*B*) Cross-sections of the point spread function at the 4 tip-sample spacings used in the imaging experiment. The PSF was calculated by using Eq. **2**, assuming $A = 1$. The color scale reflects the force variance per spin (zN = zeptonewton = 10^{-21} N). The size of the tip apex (r_a = 100 nm) is indicated by a dotted circle. At $z = 24$ nm, the PSF lobe thickness reaches a minimum of ≈4.8 nm (FWHM). The small left–right asymmetry is due to a slight (1.7°) tilt of the sample plane with respect to the magnetic tip.

improves the estimate successively by using the following steps (34, 35):

$$\delta\xi_n(\mathbf{r}_s) = \xi(\mathbf{r}_s) - \int_{\substack{\text{sample}\\ \text{volume}}} d^3\mathbf{r}\, K(\mathbf{r}_s - \mathbf{r})\rho_n(\mathbf{r}), \qquad [3]$$

$$\rho_{n+1}(\mathbf{r}) = \rho_n(\mathbf{r}) + \alpha(\mathbf{r}) \int_{\substack{\text{scan}\\ \text{volume}}} d^3\mathbf{r}_s\, K(\mathbf{r}_s - \mathbf{r})\delta\xi_n(\mathbf{r}_s), \qquad [4]$$

where $\rho_n(\mathbf{r})$ is the reconstructed spin density after n iterations, $\delta\xi_n(\mathbf{r}_s)$ is the difference between the measured and predicted spin signal maps (the error to be minimized), and $\alpha(\mathbf{r})$ controls the rate of convergence. Because spin density should always be ≥ 0, we enforce this condition by setting any negative values of $\rho_n(\mathbf{r})$ to zero after each iteration step. The iterations typically proceed for a few thousand steps until the residual error becomes comparable with the measurement noise. In the future, the implementation of more sophisticated image reconstruction algorithms may be advantageous (36).

Results

Fig. 3A shows 3D scan data organized as *x*–*y* scans taken at 4 different tip-sample spacings: d = 24, 37, 50, and 62 nm. Each of the approximately 50-nm × 50-nm scan areas contains 60 × 32 data points acquired with an acquisition time of 1 min per point. Peak signal strength ranged from ≈600 aN^2 for the closest scan plane to ≈90 aN^2 at the most distant plane. The uncertainty of the spin signal estimate (the standard error of the measurement) ranges from ≈40 aN^2 for the d = 24 nm scan plane to ≈15 aN^2 for d = 62 nm. Thus, at the positions of maximum signal, the signal-to-noise ratio (SNR) varied from ≈15 for the closest scan plane to ≈6 at the most distant plane.

The correlation time τ_m of the spin signal was estimated from the signal bandwidth and found to be quite short, on the order of 20 ms. This is significantly shorter than has been seen in some inorganic test samples (26), possibly because of a naturally short rotating frame relaxation time $T_{1\rho}$.

An indication of the spatial resolution inherent in the raw data can be seen in the line scan shown in Fig. 3*B*. The line scan, taken with d = 24 nm tip-sample spacing, shows a background spin signal of ≈300 aN^2, with signal peaks up to ≈600 aN^2. The leading edges of the peaks are sharp and indicate that the resolution in the x direction (before deconvolution) is on the order of 4 nm, which is approximately the thickness of the resonant slice (Fig. 2*B*).

Perhaps the most striking aspects of Fig. 3*A* are the apparent "double" images in each of the *x*–*y* scans. This feature doubling effect is due to the 2-lobed character of the PSF (Fig. 2*B*). As expected, the feature pairs are seen to move apart as the tip-sample spacing decreases.

The signal information from the 4 scan planes (together with a fifth "zero" plane at d = 75 nm, where no signal was found to be present) constitutes a 3D dataset that can be deconvolved to find the real-space image of the spin density. The result of the deconvolution is displayed in Fig. 3*C*, which shows the calculated spin density of the sample as a series of *x*–*y* planes at various z positions. A representative *x*–*y* plane is highlighted in Fig. 3*D* and clearly shows an assembly of a few individual virus particles (mostly fragments). Given that the raw MRFM data are spatially undersampled and have only modest SNR, the quality of the reconstruction is remarkable. The observation of significant improvement in image SNR after reconstruction is expected because most spins contribute force signal to more than one position in the scan, and the cumulative effect benefits the SNR of the reconstruction. The resolution appears to be in the 4- to 10-nm range, depending on the direction, with the x direction having the highest resolution. This resolution anisotropy is expected because of the directional dependence of the PSF, which reflects the fact that the cantilever responds only to the x component of magnetic force.

The fidelity of the MRFM reconstruction is confirmed by comparing the results in Fig. 3*D* to the scanning electron microscope (SEM) image of the same sample region (Fig. 3*E*). Excellent agreement is found even down to small details. Note that the origin of contrast in the 2 images is qualitatively very different. The MRFM reconstruction is elementally specific and shows the 3D distribution of hydrogen in the sample. Contrast in the SEM image is mainly due to the virus blocking the secondary electrons emitted from the underlying gold-coated cantilever surface.

The depth resolution that is enabled by the 3D image reconstruction is illustrated in Fig. 3*F*, which shows a vertical cross-section that extends through 2 virus fragments. Interestingly, the cross-sectional cut reveals that the virus particles sit on top of a thin layer of proton-containing material that is not visible by SEM. The presence of this background layer is not surprising because it is well known that surfaces that have been exposed to ordinary laboratory air become coated with a thin layer of adsorbed hydrocarbons and water. It is this proton-rich layer that is responsible for the 300 aN^2 baseline signal in Fig. 3*B*. Taking this baseline signal level, combined with knowledge of the point-spread function and the typical spin density of hydrocarbons, one can estimate the layer thickness. Assuming a hydrocarbon spin density of $\rho = 7 \times 10^{28}$ spins per m^3, the layer thickness is on the order of a nanometer.

The reconstructions shown in Fig. 3 *C*, *D*, and *F* use no a priori knowledge of the imaged object, such as the presence of the

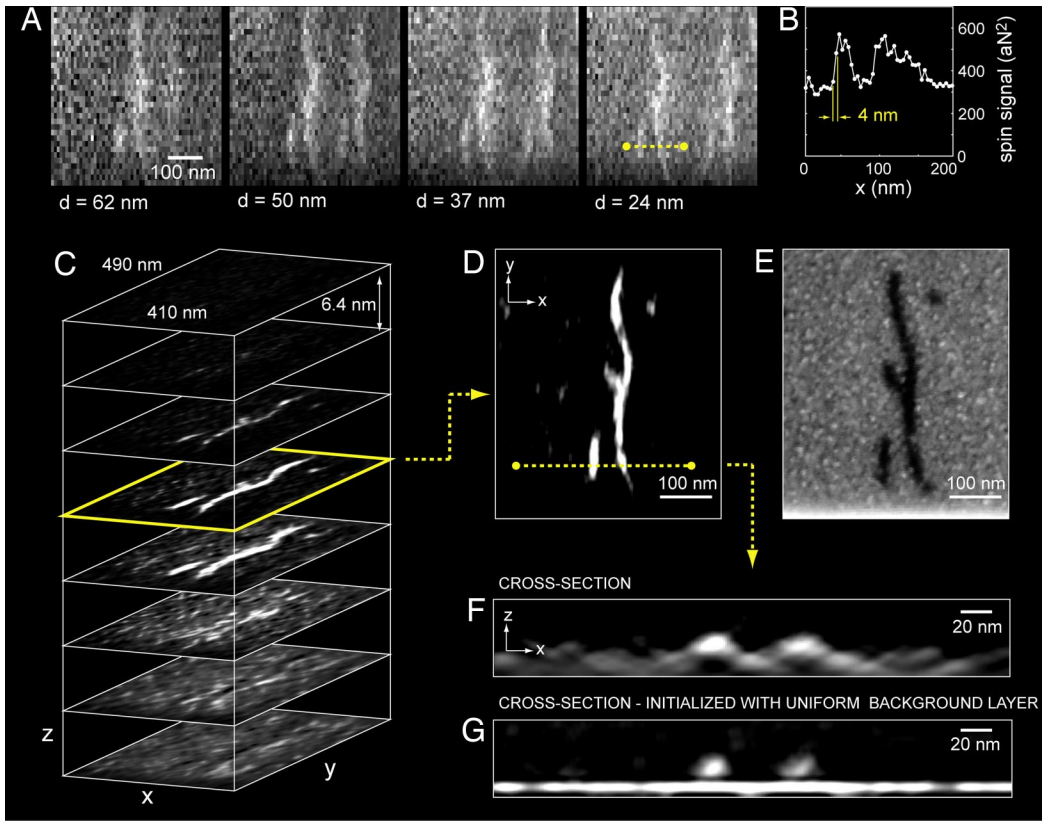

Fig. 3. Spin signal scan data and resulting 3D reconstruction of the hydrogen (proton) density distribution. (*A*) Raw scan data presented as *x*–*y* scans of the spin signal at 4 different tip-sample spacings. Pixel spacing is 8.3 nm × 16.6 nm in *x* × *y*, respectively. Each data point represents the spin signal variance obtained during a 1-min integration. B_{ext} = 2.482 T. (*B*) A more finely sampled line scan showing 4-nm lateral resolution. The scanned region is indicated by the dashed line in *A*. B_{ext} = 2.432 T. (*C*) Reconstructed 3D ^{1}H spin density. Black represents very low or zero density of hydrogen, whereas white is high hydrogen density. The image is the result of the Landweber reconstruction, followed by a 5-nm smoothing filter. (*D*) Horizontal slice of *C*, showing several TMV fragments. (*E*) Scanning electron micrograph of the same region. (*F*) Cross-section showing 2 TMV particles on top of a hydrogen-rich background layer adsorbed on the Au surface. (*G*) Reconstruction is improved if this background layer is included as a priori information by assuming a thin, uniform plane of ^{1}H density as the starting point of the reconstruction.

adsorbate layer on the sample. We find that the inclusion of this information into our initial guess of the spin density ρ_0 substantially improves the result of the reconstruction. For Fig. 3*G*, we initialize ρ_0 with a uniform layer of material positioned at the level of the cantilever surface, just below the virus particle. As seen in the figure, this modification allows for a much better separation of the background layer and more clearly resolves the TMV particles. Such constraints on ρ_0 (or ρ) offer a general way to systematically include known structural information about the object.

A second MRFM image reconstruction from a neighboring sample area is shown in Fig. 4. Again, a clear 3D view of the hydrogen distribution is seen, including good spatial discrimination between the virus particles and the underlying adsorbed layer.

Discussion

We believe the present work represents substantial progress in developing the capability to probe the 3D chemical/elemental composition of nanostructures. With further progress in resolution and sample preparation, force-detected MRI techniques could have significant impact on the imaging of nanoscale biological structures, even down to the scale of individual molecules. Achieving resolution <1 nm seems realistic because the current apparatus operates almost a factor of 10 away from the best demonstrated force sensitivities (37) and field gradients (38).

Even with a resolution >1 nm, MRFM may allow the basic structure of large molecular assemblies to be elucidated. One can imagine enhancing MRFM image contrast beyond the basic spin-density information by using techniques similar to those developed for clinical MRI and NMR spectroscopy. Such contrast may include selective isotopic labeling (for example, substituting ^{1}H with ^{2}H), selective imaging of different chemical

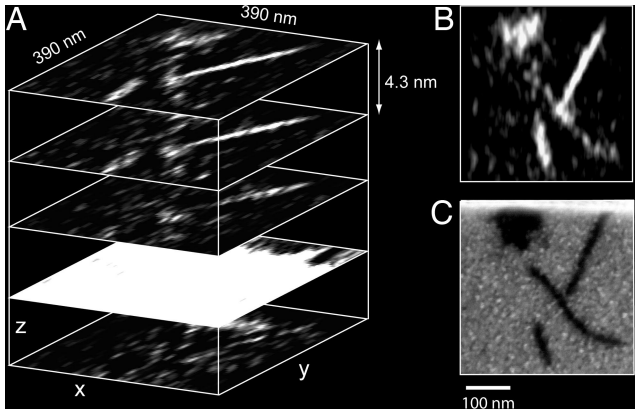

Fig. 4. Imaging results for a second sample region. (*A*) Three-dimensional reconstruction of ^{1}H spin density for virus particles sitting on adsorbed layer of hydrocarbons. (*B*) Representative horizontal slice from the 3D reconstruction showing the distribution of hydrogen in the plane located 13 nm above the hydrocarbon layer. Several virus particles are evident. (*C*) Corresponding scanning electron micrograph.

species (like ^{13}C, ^{15}N, or ^{31}P), relaxation-weighted imaging, and spectroscopic imaging that reflects the local chemical environment (20, 39). Some techniques, such as cross-polarization and depolarization between different nuclear spin species, have already been demonstrated for MRFM on the micrometer scale (21, 22). At the nanometer scale, the ability to target and locate specific proteins although selective labeling, for example, could allow direct 3D imaging of the organization and structure of multicomponent macromolecular complexes. Such a capability would be complementary to current techniques, such as cryo-electron microscopy, and could develop into a powerful tool for structural biology.

ACKNOWLEDGMENTS. We thank C. Micheel, G. Wallraff, J. Cha, and S. Swanson for help with sample preparation; J. Frommer for AFM support; M. Hart and M. Farinelli for fabrication of the microwire and magnetic tip; M. Ting and A. Hero for discussions on image reconstruction; and B. Chui for cantilever fabrication. This work was supported by IBM and the National Science Foundation-funded Center for Probing the Nanoscale (National Science Foundation Grant Number PHY-0425897). C.L.D. acknowledges support from the Swiss National Science Foundation.

1. Mansfield P (2004) Snapshot magnetic resonance imaging (Nobel lecture). *Angew Chem Int Ed Engl* 43:5456–5464.
2. Buxton RB (2002) *Introduction to Functional Magnetic Resonance Imaging: Principles and Techniques* (Cambridge Univ Press, Cambridge, UK).
3. Callaghan PT (1991) *Principles of Nuclear Magnetic Resonance Microscopy* (Oxford Univ Press, Oxford), pp 173–226.
4. Glover P, Mansfield P (2002) Limits to magnetic resonance microscopy. *Rep Prog Phys* 65:1489–1511.
5. Lee SC, *et al.* (2001) One micrometer resolution NMR microscopy. *J Magn Reson* 150:207–213.
6. Ciobanu L, Seeber DA, Pennington CH (2002) 3D MR microscopy with resolution 3.7 μm by 3.3 μm by 3.3 μm. *J Magn Reson* 158:178–182.
7. Ciobanu L, Webb AG, Pennington CH (2003) Magnetic resonance imaging of biological cells. *Prog Nucl Magn Reson Spectrosc* 42:69–93.
8. Tyszka JM, Fraser SE, Jacobs RE (2005) Magnetic resonance microscopy: Recent advances and applications. *Curr Opin Biotechnol* 16:93–99.
9. Sidles JA, *et al.* (1995) Magnetic resonance force microscopy. *Rev Mod Phys* 67:249–265.
10. Sidles JA (1992) Folded Stern–Gerlach experiment as a means for detecting nuclear magnetic resonance in individual nuclei. *Phys Rev Lett* 68:1124–1127.
11. Rugar D, Yannoni CS, Sidles JA (1992) Mechanical detection of magnetic resonance. *Nature* 360:563–566.
12. Rugar D, *et al.* (1994) Force detection of nuclear magnetic resonance. *Science* 264:1560–1563.
13. Zhang Z, Hammel PC, Wigen PE (1996) Observation of ferromagnetic resonance in a microscopic sample using magnetic resonance force microscopy. *Appl Phys Lett* 68:2005–2007.
14. Rugar D, Budakian R, Mamin HJ, Chui BW (2004) Single spin detection by magnetic resonance force microscopy. *Nature* 430:329–332.
15. Züger O, Hoen ST, Yannoni CS, Rugar D (1996) Three-dimensional imaging with a nuclear magnetic resonance force microscope. *J Appl Phys* 79:1881–1884.
16. Klein O, Naletov VV, Alloul H (2000) Mechanical detection of nuclear spin relaxation in a micron-size crystal. *Eur Phys J B* 17:57–68.
17. Thurber KR, Harrell LE, Smith DD (2003) 170nm nuclear magnetic resonance imaging using magnetic resonance force microscopy. *J Magn Reson* 162:336–340.
18. Garner SR, *et al.* (2004) Force-gradient detected nuclear magnetic resonance. *Appl Phys Lett* 84:5091–5093.
19. Mamin HJ, Budakian R, Chui BW, Rugar D (2005) Magnetic resonance force microscopy of nuclear spins: Detection and manipulation of statistical polarization. *Phys Rev B* 72:024413.
20. Degen CL, *et al.* (2005) Microscale localized spectroscopy with a magnetic resonance force microscope. *Phys Rev Lett* 94:207601.
21. Lin Q, *et al.* (2006) Magnetic double resonance in force microscopy. *Phys Rev Lett* 96:137604.
22. Eberhardt KW, Lin Q, Meier U, Hunkeler A, Meier BH (2007) Sensitive magnetic resonance force imaging of low-gamma nuclei. *Phys Rev B* 75:184430.
23. Degen CL, Poggio M, Mamin HJ, Rugar D (2007) Role of spin noise in the detection of nanoscale ensembles of nuclear spins. *Phys Rev Lett* 99:250601.
24. Kuehn S, Hickman SA, Marohn JA (2008) Advances in mechanical detection of magnetic resonance. *J Chem Phys* 128:052208.
25. Mamin HJ, Poggio M, Degen CL, Rugar D (2007) Nuclear magnetic resonance imaging with 90-nm resolution. *Nat Nanotechnol* 2:301–306.
26. Poggio M, Degen CL, Rettner CT, Mamin HJ, Rugar D (2007) Nuclear magnetic resonance force microscopy with a microwire RF source. *Appl Phys Lett* 90:263111.
27. Caspar DLD (1963) Assembly and stability of the tobacco mosaic virus particle. *Adv Protein Chem* 18:37–121.
28. Klug A (1999) The tobacco mosaic virus particle: Structure and assembly. *Philos Trans R Soc London Ser B* 354:531–535.
29. Taylor KA, Glaeser RM (1974) Electron diffraction of frozen-hydrated protein crystals. *Science* 186:1036–1037.
30. Adrian M, Dubochet J, Lepault J, McDowall AW (1984) Cryo-electron microscopy of viruses. *Nature* 308:32–36.
31. Sleator T, Hahn EL, Hilbert C, Clarke J (1985) Nuclear spin noise. *Phys Rev Lett* 55:1742–1745.
32. Crooker SA, Rickel DG, Balatsky AV, Smith DL (2004) Spectroscopy of spontaneous spin noise as a probe of spin dynamics and magnetic resonance. *Nature* 431:49–52.
33. Müller N, Jerschow A (2006) Nuclear spin noise imaging. *Proc Natl Acad Sci USA* 103:6790–6792.
34. Bertero M, Boccacci P (1998) *Introduction to Inverse Problems in Imaging* (Institute of Physics, Bristol, UK), pp 137–167.
35. Chao S, Dougherty WM, Garbini JL, Sidles JA (2004) Nanometer-scale magnetic resonance imaging. *Rev Sci Instr* 75:1175–1181.
36. Ting M, Raich R, Hero AO (2006) Sparse image reconstruction using sparse priors. *Proceedings of 2006 IEEE Intl. Conf. on Image Processing* (IEEP, Piscataway, NJ).
37. Mamin HJ, Rugar D (2001) Sub-attonewton force detection at millikelvin temperatures. *Appl Phys Lett* 79:3358–3360.
38. Tsang C, *et al.* (2006) Head challenges for perpendicular recording at high areal density. *IEEE Trans Magn* 42:145–149.
39. Haacke EM, Brown RW, Thompson MR, Venkatesan R (1999) *Magnetic Resonance Imaging: Physical Principles and Sequence Design* (Wiley, New York), pp 331–380.

Supporting Information - Appendix

Nanoscale magnetic resonance imaging

C. L. Degen[1], M. Poggio[1,2], H. J. Mamin[1] , C. T. Rettner[1] and D. Rugar[1]

[1]*IBM Research Division, Almaden Research Center, San Jose, CA 95120, USA.*

[2]*Center for Probing the Nanoscale, Stanford University, Stanford, CA 94305, USA.*

1. MRFM apparatus

The MRFM apparatus is located in a small vacuum chamber ($p<10^{-6}$ mbar) attached to the mixing chamber of a dilution refrigerator and cooled to the operating base temperature of 300 mK. A spring-based isolation system serves to decouple the apparatus from environmental vibrations. The mass-loaded, single-crystal silicon cantilever has an overall length of 120 μm, with a flexible shaft that is 3 μm wide and 100 nm thick (*1*). The silicon mass located at the end of the cantilever is approximately 1.3 μm thick. The motion of the cantilever is detected using a fiber-optic interferometer (25 nW laser power, λ = 1550 nm). The cantilever has resonance frequency f_c = 2.9 kHz, intrinsic quality factor Q = 30,000 and spring constant k = 86 μN/m. Under measurement conditions (*i.e.*, at 2.482 T external field with the cantilever end positioned within 30 nm of the magnetic tip), the *Q*-factor drops to a few thousand. Active damping using feedback further lowers the effective *Q* to about 300 and speeds up the cantilever response time to ~30 ms (*2, 3*). The resulting force noise was in the range of 5 – 10 aN/Hz$^{1/2}$, depending on the specific positioning of the cantilever over the magnetic tip.

The Cu microwire is 2.6 μm long, 1.0 μm wide, and 200 nm thick. It generates an rf field strength $B_{rf} \approx 3$ mT at the center frequency $\omega_0 / 2\pi = 114.8$ MHz when using an rf current of 15 mA. Power dissipation is about 200 μW. The magnetic tip on the microwire is fabricated using electron beam lithography and a lift-off process. The tip material is deposited by electron beam evaporation and consists of the stack 15 nm Ti / 200 nm $Fe_{70}Co_{30}$ / 15 nm Au. The top Au layer serves to inhibit oxidation of the magnetic FeCo layer. Additional details are available in Ref. (*4*).

2. TMV sample preparation

Purified tobacco mosaic virus (TMV) was purchased from ATCC (catalog number PV-135p) at a concentration of 2,000 μg/ml in a 0.01 M phosphate buffered saline (1x PBS, pH 7.2) and then diluted with additional 1x PBS buffer to 400 μg/ml. The mass-loaded end of the cantilever was prepared by first using a focused ion beam (FIB) to create a flat sample platform about 0.8 μm wide and 1.3 μm high (Fig. 1B). The platform was then coated with 10 nm of Si and 30 nm Au by thermal evaporation. The Au film serves as an electrostatic shield to minimize force noise and is found to promote the adhesion of virus particles. Just before depositing the TMV particles, the cantilever is cleaned by UV/ozone (Bioforce Nanosciences ProCleaner) for 20 minutes in order to remove any organic surface contamination. UV/ozone cleaning renders the Au surface temporarily hydrophilic, which facilitates wetting with the aqueous TMV solution and greatly improves virus particle adhesion. We then dip the cantilever tip into a 10 μl droplet of TMV solution for 2 minutes, retract it and allow it to air dry. For dipping we use a mechanical manipulator stage to approach the cantilever tip vertically towards the droplet with the cantilever's shaft oriented normal to the droplet surface. The tip then enters the solution about 10 μm deep, such that only the very end of the cantilever is

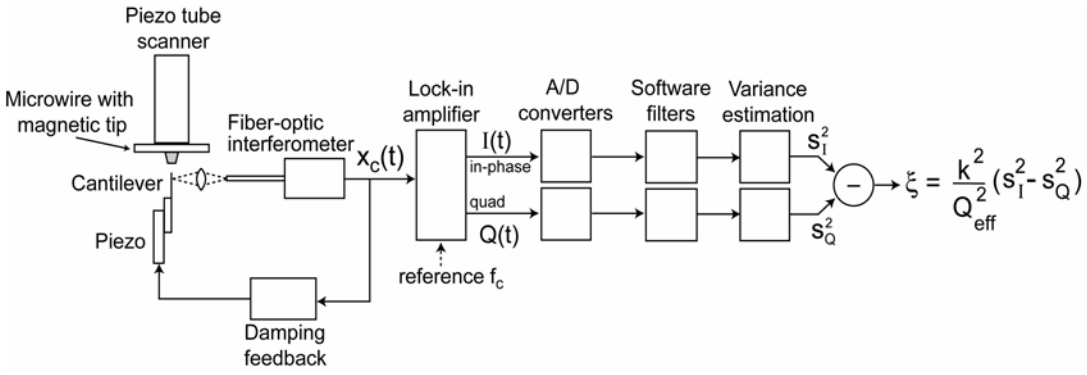

Figure S1 - Key elements for signal detection. Cantilever motion is monitored via a fiber optic interferometer and synchronously detected using a dual-phase lock-in amplifier. The lock-in output is filtered and the spin signal ξ is found by taking the difference of the variances of the in-phase and quadrature waveforms.

exposed to the virus solution. The cantilever with TMV was stored in a dry nitrogen atmosphere for several days before mounting in the MRFM apparatus.

3. Signal generation and detection

Key elements of the MRFM signal detection system are shown schematically in Figure S1. The virus sample is attached to the end of the cantilever, which is positioned close to the magnetic tip. The tip and the integrated microwire are mounted on a piezoelectric tube scanner, which scans the magnetic tip relative to the sample in three dimensions. The cantilever position $x_c(t)$ measured by the interferometer (*5*) is fed into a two-channel lock-in amplifier in order to detect the in-phase and quadrature amplitudes of the cantilever oscillation. The lock-in reference is at the cantilever resonance frequency f_c (approximately 2.9 kHz) and synchronized with the rf frequency modulation that drives cyclic inversions of the protons in the sample. In order to track changes in cantilever frequency during the scan, the cantilever frequency is measured at each scan position while briefly "self-oscillating" the cantilever (*6*).

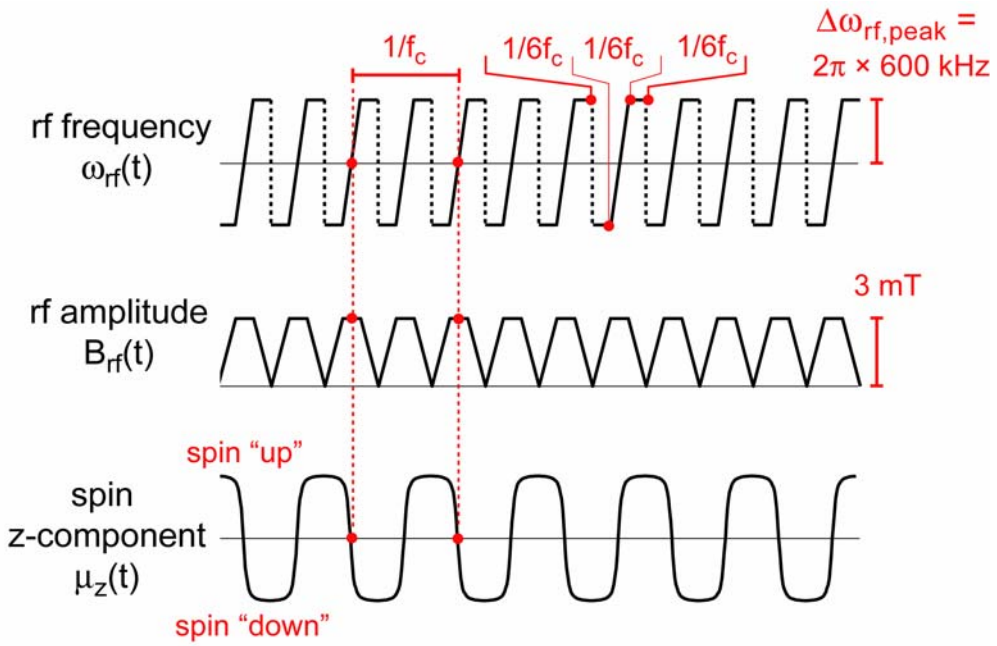

Figure S2 – rf modulation waveforms used to cyclically invert the spins. Cyclic adiabatic inversion is accomplished by sweeping the rf frequency through magnetic resonance twice per cantilever period.

The spins are cyclically inverted using the rf frequency modulation shown in Fig. S2. The rf frequency modulation $\omega_{rf}(t) = \omega_0 + \Delta\omega_{rf}(t)$ consists of unidirectional frequency sweeps (*7*, *8*) with peak deviation $\Delta\omega_{\text{rf, peak}} = 2\pi \times 600$ kHz and repetition rate $2f_c$ (i.e., two spin inversions constitute one full inversion cycle). The sweep duration is 1/6 of a cantilever cycle. A short duration is advantageous since it results in less phase shift in the cyclic inversion for off-resonance spins. The duration cannot be shortened too much, however, without causing problems with adiabaticity. The amplitude of the rf field is strongest during the frequency sweep and ramped to zero at the end of the sweep. This gives more complete inversions for spins that are not centered in the resonant slice and reduces relaxation effects associated with the sudden switching of rf frequency (*8*, *9*). The peak amplitude $B_{rf} \approx 3$ mT is large enough to satisfy the adiabatic condition, $\gamma^2 B_{rf}^2 >> \mathrm{d}\omega_{rf}/\mathrm{d}t$, so that the correlation time of the spins during the

manipulation ($\tau_m \approx 20$ ms) is set by intrinsic spin relaxation effects, and not by the details of the rf protocol, at least for the spins centered in the resonant slice.

The cyclic spin inversions generate an oscillatory attonewton force that excites the cantilever at the mechanical resonance frequency. Typical signal vibration amplitude is a fraction of an angstrom, which is somewhat smaller than the rms amplitude of cantilever thermal vibrations. The lock-in amplifier phase is set so that the spin signal appears predominantly in the in-phase channel for on-resonance spins.

Since the signal originates from the statistical (random) polarization of the spins, the sign of the detected signal can be either positive or negative and fluctuates during the course of the measurement, making conventional signal averaging ineffective. Instead, as discussed in Ref. (*7*), the spin signal is detected via its variance. To estimate the spin signal variance and to distinguish the spin signal from cantilever thermal vibrations, both the in-phase channel $I(t)$ and the quadrature channel $Q(t)$ of the lock-in amplifier are digitized. These signals are then digitally filtered in software using second-order Butterworth filters ($\tau_c = 10$ ms), and the variances s_I^2 and s_Q^2 are calculated.

The cantilever thermal noise contributes equally to s_I^2 and s_Q^2, while the spin signal predominantly adds to s_I^2. The spin signal variance is thus estimated by the difference between the in-phase and quadrature variances (*7*)

$$\xi = \frac{k^2}{Q_{\text{eff}}^2}\left(s_I^2 - s_Q^2\right), \tag{S1}$$

where the factor k^2 / Q_{eff}^2 puts the spin signal variance into units of force squared (e.g., aN^2). We refer to this detected quantity as the "spin variance signal", or simply the "spin signal".

4. Point spread function

Knowledge of the point spread function (PSF), denoted by $K(\mathbf{r})$, is key to understanding MRFM imaging behaviour and central to successful image reconstruction. $K(\mathbf{r})$ is defined as the mean MRFM signal generated by a randomly polarized spin in the sample at a position $\mathbf{r}$ with respect to the magnetic tip. The signal strength is determined by two main factors: 1) the tip field gradient $G \equiv \partial B_z / \partial x$ at the position of the spin, and 2) the effectiveness of the cyclic spin inversions for driving the cantilever vibration. The effectiveness of the spin inversions depends strongly on the position of the spin with respect to resonant slice since spins that are off resonance will not undergo full inversions and the inversion process may be less coherent.

Although a rigorous theory for the point spread function is beyond the scope of this paper, reasonable estimates can be made using some simple models. The key is to understand the off-resonance behaviour of the spin modulation. We start by considering the ideal case where a spin is cyclically inverted by following the effective field in the rotating frame. We then examine a somewhat more sophisticated model based on a numerical simulation of a cantilever coupled to a spin where the spin dynamics are governed by the Bloch equations.

A. Effective field model

The simplest model for adiabatic inversion assumes that the spin follows the effective field in the "rotating frame" – i.e., the reference frame that rotates synchronously with the rf field (*10, 11*). In our case, the effective field is position dependent and can be written as

$$\mathbf{B}_{\text{eff}}(t,\mathbf{r}) = B_{rf}(t)\hat{\mathbf{x}} + \left[\Delta B_0(\mathbf{r}) - \Delta\omega_{rf}(t)/\gamma\right]\hat{\mathbf{z}}, \qquad \text{(S2)}$$

where $B_{rf}(t)$ is the rotating frame rf field amplitude, $\Delta B_0(\mathbf{r}) = B_0(\mathbf{r}) - \omega_0/\gamma$ is the resonance offset, and $B_0(\mathbf{r})$ is the total static field (tip field plus external field). During the frequency modulation, $\mathbf{B}_{\text{eff}}$ changes its orientation with time, and the spin will follow this orientation if the angular rate of change satisfies the adiabatic condition

$$\left|\mathrm{d}\alpha/\mathrm{d}t\right| << \left|\gamma \mathbf{B}_{\text{eff}}\right| \tag{S3}$$

where

$$\alpha(t,\mathbf{r}) = \arctan\left[\frac{B_{rf}(t)}{\Delta B_0(\mathbf{r}) - \Delta\omega_{rf}(t)/\gamma}\right] \tag{S4}$$

Assuming that the spin and effective field are initially aligned or anti-aligned, the z component of the spin magnetic moment during the frequency modulation can then be written as

$$\mu_z(t,\mathbf{r}) = \pm\mu \frac{\Delta B_0(\mathbf{r}) - \Delta\omega_{rf}(t)/\gamma}{\left[\left(B_{rf}(t)\right)^2 + \left(\Delta B_0(\mathbf{r}) - \Delta\omega_{rf}(t)/\gamma\right)^2\right]^{1/2}} \tag{S5}$$

where μ is the proton magnetic moment. The plus sign signifies alignment between the spin and the effective field ("spin locked" case), while the minus sign signifies anti-alignment ("spin anti-locked").

Figure S3A shows waveforms of $\mu_z(t)$ for various values of the off-resonance condition ΔB_0, assuming that the frequency and amplitude modulation are that shown in Fig. S2. We assume a peak frequency deviation of 600 kHz ($\Delta B_{peak} \equiv \Delta\omega_{rf,peak}/\gamma = 14$ mT) and an rf amplitude modulation that ranges from zero to a maximum strength of 3 mT. For the on-resonance case ($\Delta B_0 = 0$), the spin undergoes very complete inversions and alternates between the spin locked and anti-locked states. As the off-resonance condition increases, the waveform shifts in time and

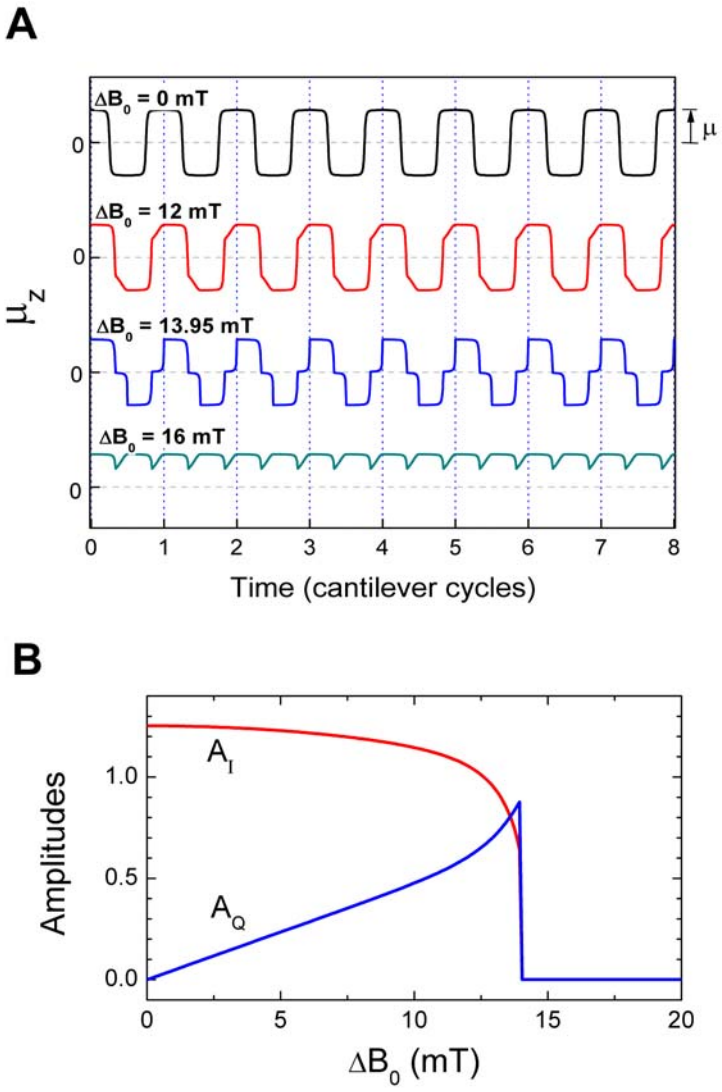

Figure S3 – Results from effective field model. (**A**) Waveforms showing z component of magnetic moment calculated using equation (S5) for various off-resonance conditions ΔB_0 . (**B**) Fourier amplitudes of in-phase (A_I) and quadrature (A_Q) components

becomes distorted. Finally, when $\Delta B_0 > \Delta B_{peak}$, the spin no longer passes through resonance and the inversion ceases.

Waveforms of the type shown in Fig. S3A have been Fourier analyzed to determine their effectiveness for driving a cantilever response. We write $\mu_z(t)$ in terms of the fundamental frequency components as $\mu_z(t) = A_I \mu \cos(\omega_c t) + A_Q \mu \sin(\omega_c t)$ and plot A_I and A_Q as a function of the off resonance condition in Fig. S3B. For small ΔB_0, A_I is of order unity and A_Q is small. As ΔB_0 approaches ΔB_{peak}, A_I diminishes, while A_Q grows. Finally, when $\Delta B_0 > \Delta B_{peak}$, both A_I and A_Q abruptly drop to zero.

The above result is for ideal classical spin behavior. In reality, the spin will undergo random spin flips between the spin-locked and anti-locked states, resulting in random polarities of A_I and A_Q. It is this randomness that necessitates the variance-based signal detection defined by equation (S1). Since the in-phase force is given by $\mu G A_I$, the variance of the in-phase force for a spin with fluctuating orientation will be proportional to $\mu^2 G^2 A_I^2$, and likewise for the quadrature force. Using the definition of the MRFM signal in (S1), which is based on the difference between the in-phase and quadrature variances, we find that the point spread function can be written as

$$K(\mathbf{r}) = A\mu^2 \left[G(\mathbf{r})\right]^2 \eta\left(\Delta B_0(\mathbf{r})\right), \tag{S6}$$

where

$$\eta(\Delta B_0) = \frac{A_I^2(\Delta B_0) - A_Q^2(\Delta B_0)}{A_I^2(0)} \tag{S7}$$

is a function characterizing the off-resonance response (normalized so that $\eta(0) = 1$). A is an overall constant, typically close to unity, that depends on the correlation time of

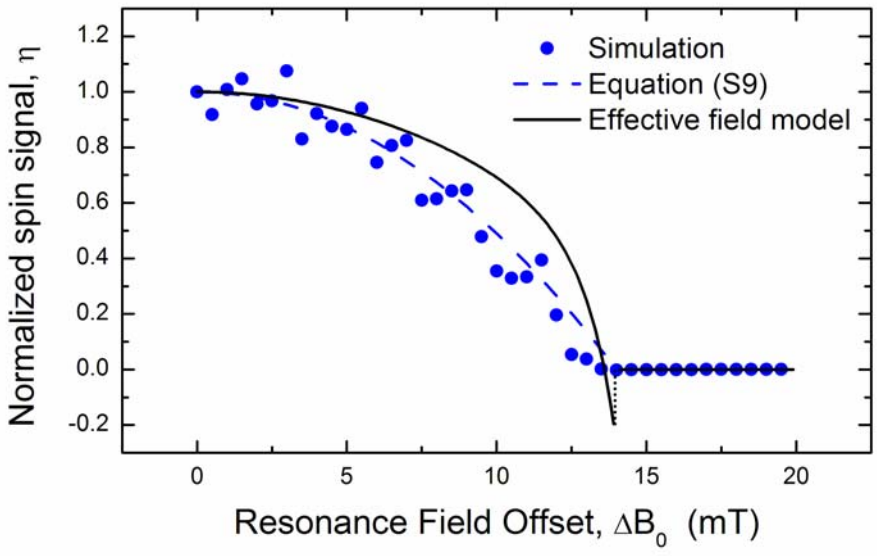

Figure S4 – Normalized spin signal as a function of resonance offset. Solid black line is based on effective field model (S5). Data points are simulation results based on the equations in (S8). The dashed line is the second-order approximation in (S9).

the statistical spin polarization, the lock-in detection bandwidth and the Fourier coefficient of the on-resonance waveform, $A_1(0)$.

A plot of $\eta(\Delta B_0)$ is shown in Fig. S4. As expected, $\eta(\Delta B_0)$ drops as ΔB_0 increases, and eventually attains negative values due to the phase shift of the cyclic inversion waveform. One aspect of the model is clearly unphysical: the discontinuous jump to zero at $\Delta B_0 = \Delta B_{peak}$. Another deficiency of this model is the assumption that the spin follows the effective field even as B_{rf} diminishes to zero due to the amplitude modulation of the rf field. One would expect the spin-lock assumption to break down for small rf field strength. To address these issues, we developed a second model for a cantilever coupled to the spin, where the spin dynamics is governed by the Bloch equations.

B. Simulation based on the Bloch equations

We treat the cantilever as a simple harmonic oscillator coupled to the z component of the spin via the gradient G. The spin dynamics are assumed to be governed by the Bloch equations without relaxation. The coupled equations are:

$$\begin{aligned}
\dot{\mu}_x &= \gamma \mu_y \left[G x_c + \Delta B_0 - \Delta\omega_{rf}(t)/\gamma \right] \\
\dot{\mu}_y &= \gamma \mu_z B_{rf}(t) - \gamma \mu_x \left[G x_c + \Delta B_0 - \Delta\omega_{rf}(t)/\gamma \right] \\
\dot{\mu}_z &= -\gamma \mu_y B_{rf}(t) \\
\ddot{x}_c &+ \frac{\omega_c}{Q_{eff}} \dot{x}_c + \omega_c^2 x_c = G\mu_z / m_c
\end{aligned} \tag{S8}$$

The rf field is assumed to be oriented in the x direction in the rotating frame with amplitude and frequency modulation specified by $B_{rf}(t)$ and $\Delta\omega_{rf}(t)$, respectively. The parameter $m_c = k/\omega_c^2$ is the effective mass of the cantilever and the term $\left[G x_c + \Delta B_0 - \Delta\omega_{rf}(t)/\gamma \right]$ represents the z component of the effective field, including the effect of the cantilever position, the off resonance condition and the rf frequency modulation. These equations were solved step-wise in time using the Runge-Kutta method in order to simulate the behaviour of a randomly oriented spin.

Since the above equations represent the dynamics of an ideal, isolated spin, one additional *ad hoc* assumption was made in the simulation in order to take into account the loss of spin lock for small rf field values. It was assumed that the phase of the spin (i.e., the orientation of the spin in the x-y plane) is randomized when B_{rf} falls below a minimum value, $B_{rf,\min}$. The most appropriate choice for $B_{rf,\min}$ is not obvious. We chose $B_{rf,\min} = 0.5$ mT since we know experimentally that the spin-lock is quite ineffective with such low rf field for protons in organic materials, presumably due to the effect of dipolar interactions. The overall effect of the phase randomization is minimal for spins that undergo full inversions (i.e., for spins that are pointed along the z axis as

B_{rf} goes to zero). However, for spins not fully inverted as the B_{rf} goes to zero, the effect is significant and leads to additional randomization of the spin orientation.

Figure S5 shows a typical simulation result where the cantilever position is plotted as a function of time. The cantilever vibration amplitude is seen to fluctuate with a characteristic correlation time on the order of 30 ms, similar to that observed experimentally. To determine the spin signal from this time record, the cantilever waveform was subjected to a software signal detector equivalent to the hardware version depicted in Fig. S1. Since the spin signal is statistical in nature, the simulation was run 100 times with random initial spin orientations in order to determine the mean signal. Each simulation calculated a 0.5 s time record. This process was repeated as a function of the off-resonance condition ΔB_0 to obtain the normalized response function $\eta(\Delta B_0)$ shown by the points in Fig. S4.

As evident in Fig. S4, both the spin simulation and the effective field model predict that $\eta(\Delta B_0)$ is maximum for $\Delta B_0 = 0$ and falls to zero when $\Delta B_0 > \Delta B_{peak}$. The simulation eliminates the unphysical discontinuity evident in the effective field model. A simple analytical expression is found to fit the simulation data very well:

$$\begin{aligned} \eta(\Delta B_0) &= \left(1 - \frac{\Delta B_0^2}{\Delta B_{peak}^2}\right) \quad \text{for } |\Delta B_0| < \Delta B_{peak} \\ &= 0 \qquad\qquad\quad \text{for } |\Delta B_0| \geq \Delta B_{peak} \end{aligned} \tag{S9}$$

We incorporate this approximation into the expression for the point spread function, yielding

$$\begin{aligned} K(\mathbf{r}) &= A\mu^2 \left[G(\mathbf{r})\right]^2 \left(1 - \frac{\left[\Delta B_0(\mathbf{r})\right]^2}{\Delta B_{peak}^2}\right) \quad \text{for } |\Delta B_0| < \Delta B_{peak} \\ &= 0 \qquad\qquad\qquad\qquad\qquad\quad \text{otherwise} \end{aligned} \tag{S10}$$

This equation is the basis of the PSF shown in Fig. 2 of the main text.

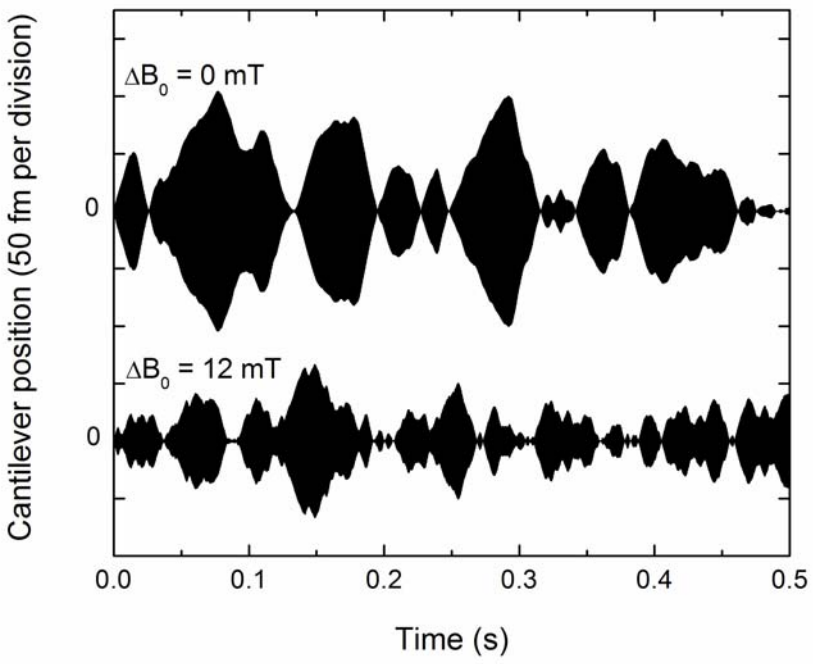

Figure S5 – Typical simulations of cantilever vibration resulting from a proton spin manipulated by the rf frequency and amplitude modulation shown in Fig. S2. The off-resonance signal is significantly smaller and has shorter correlation time. The simulation parameters closely matched those of the experiment: Q_{eff} = 300, $k = 86\ \mu$N/m , $f_c = 2.9$ kHz, $G = 3$ MT/m, $B_{rf} = 3$ mT and $B_{rf,\min} = 0.5$ mT .

5. Magnetic tip model

The point spread function (S10) requires knowledge of the tip field and the tip field gradient. We model the tip as a uniformly magnetized truncated cone with apex radius r_a, base radius r_b and height h. The tip is assumed to be magnetized along the cone axis in the *z* direction with saturation magnetization M_s. On top of the truncated cone, we assume there is a non-magnetic surface layer of thickness *s*, which accounts for the protective overcoat (15 nm of gold) plus a possible additional non-magnetic "dead" layer. The magnetic field from the tip can be calculated by using standard techniques, such as integrating the field from the equivalent surface currents (*12*).

The tip is assumed to be centered about the *z* axis with the topmost (non-magnetic) layer extending up to the plane $z = 0$. The magnetic portion of the tip extends from the base located at $z = -h - s$ to the apex located at $z = -s$. With this geometry, the radial and longitudinal field components are then given by

$$B_r(r,z) = \frac{\mu_0 M_s}{2\pi} \int_{-h-s}^{-s} \frac{z - z'}{r\left[\left(R(z')+r\right)^2 + \left(z-z'\right)^2\right]^{1/2}} \left[\frac{R^2(z') + r^2 + \left(z-z'\right)^2}{\left(R(z')-r\right)^2 + \left(z-z'\right)^2} E(q) - K(q)\right] \mathrm{d}z' \quad \text{(S11)}$$

and

$$B_z(r,z) = \frac{\mu_0 M_s}{2\pi} \int_{-h-s}^{-s} \frac{1}{\left[\left(R(z')+r\right)^2 + \left(z-z'\right)^2\right]^{1/2}} \left[\frac{R^2(z') - r^2 - \left(z-z'\right)^2}{\left(R(z')-r\right)^2 + \left(z-z'\right)^2} E(q) + K(q)\right] \mathrm{d}z' \quad \text{(S12)}$$

Here $R(z') = \frac{r_a - r_b}{h}(z' + s) + r_a$ defines the cone radius for z' from $-h-s$ to $-s$. $E(q)$ and $K(q)$ are the complete elliptic integrals of the first and second kind:

$$K(q) = \int_0^{\pi/2} \frac{\mathrm{d}\theta}{\sqrt{1 - q^2 \sin^2\theta}} \tag{S13}$$

$$E(q) = \int_0^{\pi/2} \sqrt{1 - q^2 \sin^2\theta}\, \mathrm{d}\theta \tag{S14}$$

where

$$q^2 = \frac{4R(z')r}{\left(R(z') + r\right)^2 + \left(z - z'\right)^2}. \tag{S15}$$

The integrals in (S11) and (S12) are easily calculated numerically in order to determine $\mathbf{B}_{\mathrm{tip}}(\mathbf{r})$. The tip field gradient $G = \partial B_z / \partial x$ can also be expressed as a one-dimensional integral that is easily calculated. The expression is a bit too unwieldy to include here, however.

Table S1 shows parameters used for the tip model. To determine these parameters, we first started with the expected saturation magnetization of $Fe_{70}Co_{30}$ ($\mu_0 M_s = 2.4$ T) and with the tip geometry known either from the fabrication process or observed by scanning electron microscopy ($r_a = 100$ nm, $r_b = 175$ nm, $h = 200$ nm and $s = 15$ nm). The field and field gradient were calculated and then used with equation (S10) to determine the point spread function $K(\mathbf{r})$. The tip parameters were then refined by noting key features of the experimental data, such as the distance between the double images in Fig. 3, and comparing them with imaging behaviour expected from the point spread function. In addition, we made a separate set of quantitative measurements of the tip field as a function of spacing by measuring the onset of the MRFM signal at various external fields and tip-sample spacings, as in Ref. (*13*).

The resulting optimized tip parameters are shown in Table S1. One significant difference between the optimized parameters and the initial parameters is that the

Table S1 - Optimized parameters of the magnetic tip

Geometry	Truncated cone magnetized along $\hat{\mathbf{z}}$
Apex radius, r_a	100 nm
Base radius, r_b	160 nm
Height, h	180 nm
Non-magnetic surface layer thickness, s	26 nm
Saturation magnetization, $\mu_0 M_s$	1.51 T
Tilt of sample platform away from tip axis	0° about $\hat{\mathbf{x}}$, -1.7° about $\hat{\mathbf{y}}$
Max. lateral gradient at 24 nm physical spacing. (50 nm magnetic spacing.)	$\left\|\partial B_z / \partial x\right\|_{\max} = 4.2 \times 10^6$ T/m
Max. vertical gradient at 24 nm physical spacing. (50 nm magnetic spacing.)	$\left\|\partial B_z / \partial z\right\|_{\max} = 5.1 \times 10^6$ T/m

saturation magnetization of the tip material is smaller than expected by about 37%. In addition, the non-magnetic surface layer appears to be about 26 nm thick, significantly larger than expected based on the 15 nm thickness of the protective Au overcoat. The reason for these discrepancies is still under investigation. It is likely that these results are at least partially due to oxidation or contamination of the FeCo alloy.

If the tip were operating without these discrepancies, the achievable gradient would be increased by a factor of two. This increase would halve the thickness of the resonant slice and give a proportionate boost to the MRFM imaging resolution. A doubling of the gradient would also quadruple the signal power per spin, which could be used to decrease the measurement time by a factor of 16 at the current spatial resolution, assuming all other factors were equal.

6. Image reconstruction using the Landweber algorithm

Image reconstruction was done numerically using our own Fortran/Labview code following the algorithm outlined by equations (3) and (4) in the main text. The scan data $\xi(\mathbf{r}_s)$ is described by a three-dimensional array where the corresponding grid spacing was 8.3 nm × 16.6 nm × 12.8 nm in $x \times y \times z$. The spin density $\rho(\mathbf{r})$ and point spread function $K(\mathbf{r})$ are described by three dimensional arrays that have grid spacing that is finer than the scan data by factors of 3, 2 and 3 in *x*, *y* and *z*, respectively. In other words, the grid spacing of the arrays for the reconstructed spin density and point spread function corresponds to 2.8 nm × 8.3 nm × 4.3 nm in $x \times y \times z$. Considerable freedom is allowed with regard to the weighting function $\alpha(\mathbf{r})$. Reasonable results are obtained by simply setting $\alpha(\mathbf{r})$ to a constant value. Some improvement was found by allowing $\alpha(z)$ to increase monotonically with *z* up to a prescribed maximum value. The Landweber iterations continued until the error between experimental scan data and the predicted scan data was reduced below 20 aN^2-rms (*i.e.*, below the experimental noise level). The number of iterations to achieve satisfactory convergence was typically a few thousand, depending on the choice for $\alpha(\mathbf{r})$.

Figures S6A and S7A show the raw experimental scan data $\xi(\mathbf{r}_s)$ for the two imaging experiments presented in Figs. 3 and 4, respectively. The figures also show the calculated scan data based on the reconstructed spin density $\rho_n(\mathbf{r}')$. As explained in the main text, the calculated scan data $\xi_n(\mathbf{r}_s)$ is found by computing the convolution integral

$$\xi_n(\mathbf{r}_s) = \int_{\substack{\text{sample} \\ \text{volume}}} \mathrm{d}^3\mathbf{r}'\, K(\mathbf{r}_s - \mathbf{r}')\rho_n(\mathbf{r}'). \qquad \text{(S16)}$$

It is evident that the reconstructions are very effective in producing calculated scan data that is in excellent agreement with the measured scan data. In both cases, the difference between experimental and calculated scan data is less than 20 aN^2-rms, which is comparable to the noise level of the experimental data. This error can be further minimized by continuing the iterations of the Landweber reconstruction, but this is at the expense of adding noise to the reconstructed object.

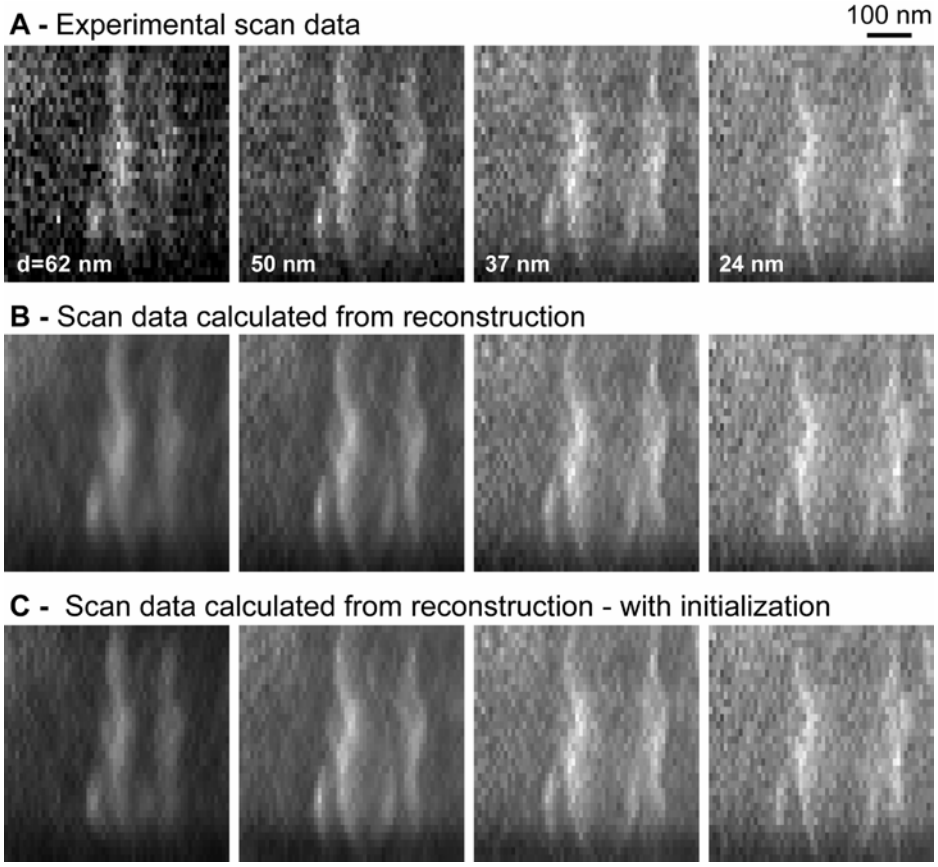

Figure S6 – Comparison of experimental scan data to the data predicted by the reconstruction. (**A**) Experimental data corresponding to Fig. 3 in the main text. Labels indicate the distances between magnetic tip and the virus particles. (**B**) Data predicted from the reconstructed spin density where initial guess in the Landweber reconstruction was zero spin density. (**C)** Same as (**B**), but with the reconstruction initialized assuming a uniform layer of proton spins on the surface.

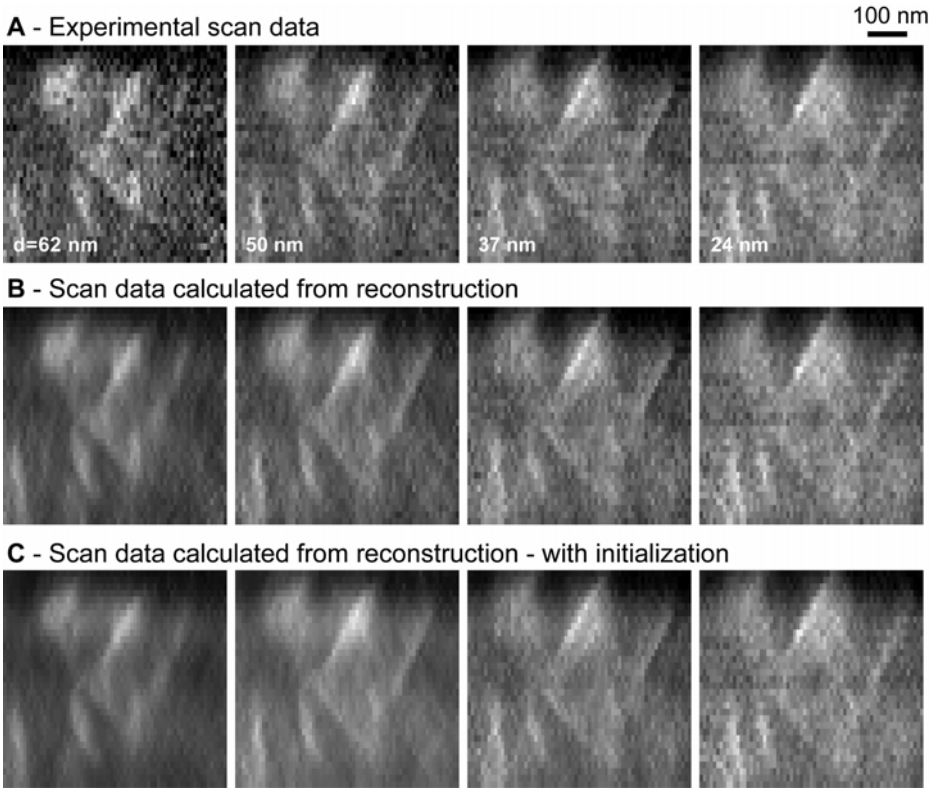

Figure S7 – Comparison of experimental scan data to the data predicted by the reconstruction. (**A**) Experimental data corresponding to Fig. 4 in the main text. Labels indicate the distances between magnetic tip and the virus particles. (**B**) Data predicted from the reconstructed spin density where initial guess in the Landweber reconstruction was zero spin density. (**C)** Same as (**B**), but with the reconstruction initialized assuming a uniform layer of proton spins on the surface.

References

1. Chui BW, Hishinuma Y, Budakian R, Mamin HJ, Kenny TW, Rugar D (2003) Mass-loaded cantilevers with suppressed higher-order modes for magnetic resonance force microscopy. *12th International Conference on Solid-State Sensors and Actuators (Transducers'03)* (IEEE, Piscataway), pp. 1120-1123.
2. Poggio M, Degen CL, Mamin HJ, Rugar D (2007) Feedback cooling of a cantilever's fundamental mode below 5mK. *Phys. Rev. Lett.* 99:017201.
3. Bruland KJ, Garbini JL, Dougherty WM, Sidles JA (1998) Optimal control of ultrasoft cantilevers for force microscopy. *J. Appl. Phys.* 83:3972-3977.
4. Poggio M, Rettner CT, Degen CL, Mamin HJ, Rugar D (2007) Nuclear magnetic resonance microscopy with a microwire rf source. *Appl. Phys. Lett.* 90:263111.
5. Rugar D, Mamin HJ, Geuthner P (1989) Improved fiber-optic interferometer for atomic force microscopy. *Appl. Phys. Lett.* 55:2588-2590.
6. Albrecht TR, Grutter P, Horne D, Rugar D (1991) Frequency-Modulation Detection Using High-Q Cantilevers for Enhanced Force Microscope Sensitivity. *J. Appl. Phys.* 69:668-673.
7. Degen CL, Poggio M, Mamin HJ, Rugar D (2007) Role of Spin Noise in the Detection of Nanoscale Ensembles of Nuclear Spins. *Phys. Rev. Lett.* 99:250601.
8. Madsen LA, Leskowitz GM, Weitekamp DP (2004) Observation of force-detected nuclear magnetic resonance in a homogeneous field. *Proc. Nat. Acad. Sci.* 101:12804-12808.

9. Degen CL (2005) Magnetic resonance force microscopy: NMR spectroscopy on the micro- and nanoscale. PhD thesis (ETH, Zurich).

10. Slichter CP (1996) *Principles of Magnetic Resonance* (Springer, Heidelberg), pp. 23-24.

11. Garwood M, DelaBarre L (2001) The return of the frequency sweep: designing adiabatic pulses for contemporary NMR. *J. Magn. Res.* 153:155-177.

12. Craik D (1997) *Magnetism - principles and applications* (Wiley, New York), pp. 334-336.

13. Mamin HJ, Poggio M, Degen CL, Rugar D (2007) Nuclear magnetic resonance imaging with 90-nm resolution. *Nature Nanotechn.* 2:301-306.

Supporting Information

Degen *et al.* 10.1073/pnas.0812068106

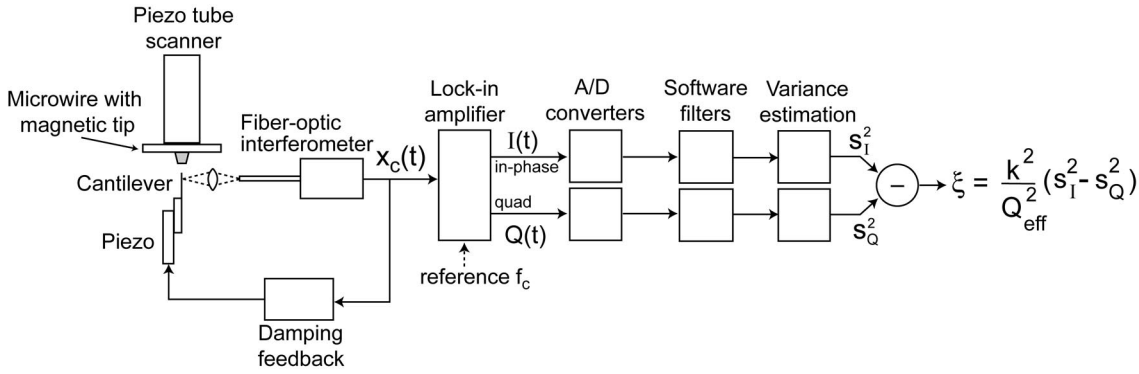

Fig. S1. Key elements for signal detection. Cantilever motion is monitored via a fiber optic interferometer and synchronously detected using a dual-phase lock-in amplifier. The lock-in output is filtered and the spin signal ξ is found by taking the difference of the variances of the in-phase and quadrature waveforms.

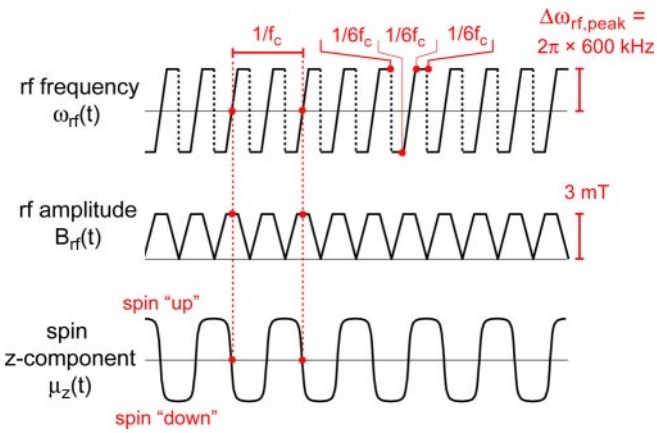

Fig. S2. rf modulation waveforms used to cyclically invert the spins. Cyclic adiabatic inversion is accomplished by sweeping the rf frequency through magnetic resonance twice per cantilever period.

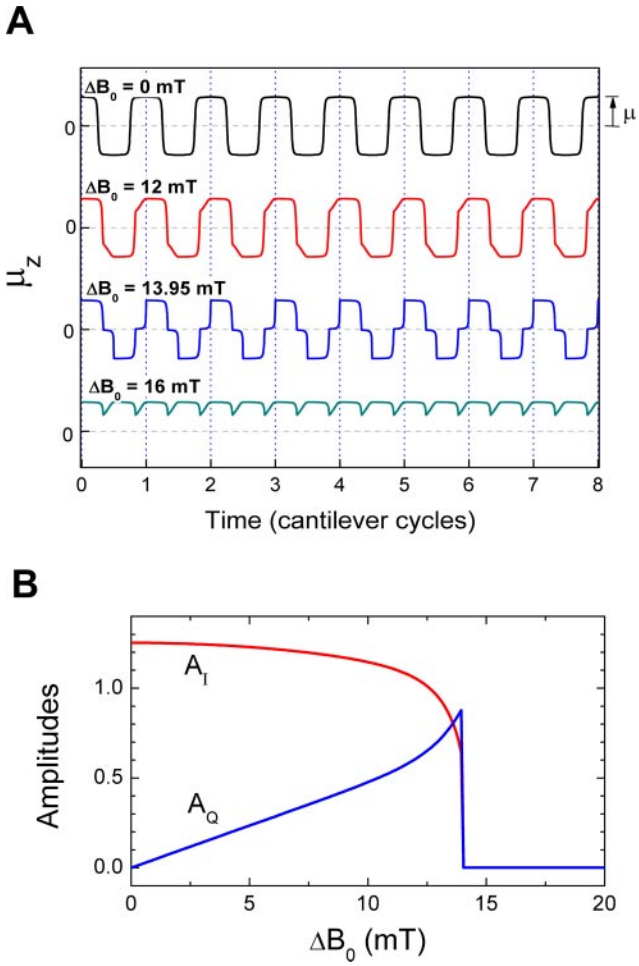

Fig. S3. Results from effective field model. (*A*) Waveforms showing *z* component of magnetic moment calculated for various off-resonance conditions ΔB_0 using Eq. **S5** (see *SI Appendix*). (*B*) Fourier amplitudes of in-phase (A_I) and quadrature (A_Q) components.

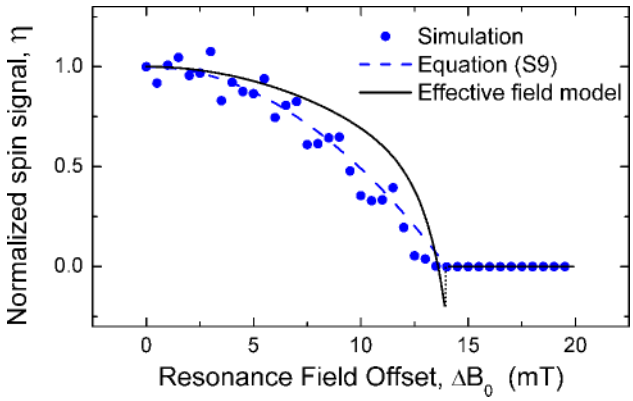

Fig. S4. Normalized spin signal as a function of resonance offset. Solid black line is based on effective field model (Eq. **S7** in *SI Appendix*). Data points are simulation results based on the equations in Eq. **S8** in *SI Appendix*. The dashed line is the second-order approximation in Eq. **S9** in *SI Appendix*.

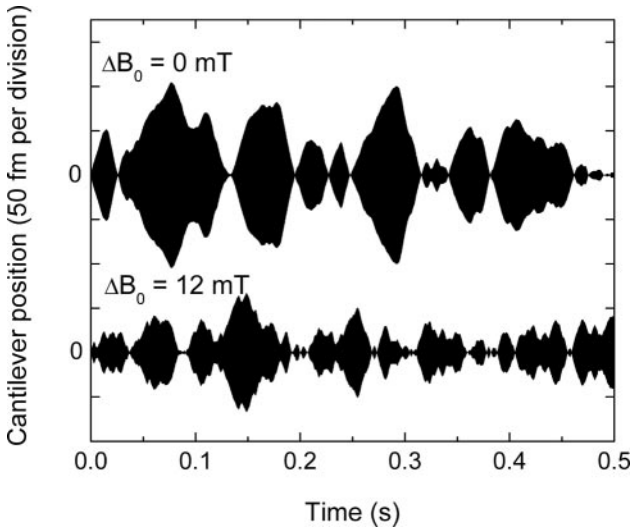

Fig. S5. Typical simulations of cantilever vibration resulting from a proton spin manipulated by the rf frequency and amplitude modulation shown in Fig. S2. The off-resonance signal is significantly smaller and has shorter correlation time. The simulation parameters closely matched those of the experiment: $Q_{\text{eff}} = 300$, $k = 86$ μN/m, $f_c = 2.9$ kHz, $G = 3$ MT/m, $B_{\text{rf}} = 3$ mT, and $B_{\text{rf,min}} = 0.5$ mT.

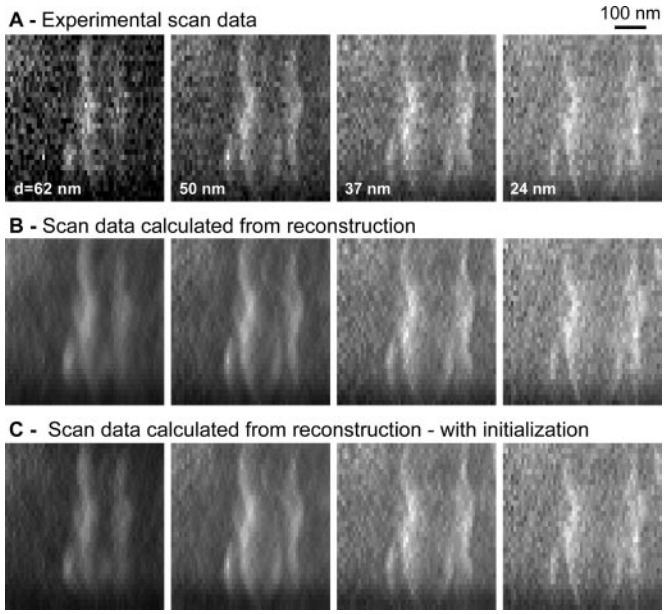

Fig. S6. Comparison of experimental scan data to the data predicted by the reconstruction. (*A*) Experimental data corresponding to Fig. 3 in the main text. Labels indicate the distances between magnetic tip and the virus particles. (*B*) Data predicted from the reconstructed spin density where initial guess in the Landweber reconstruction was zero spin density. (*C*) Same as *B*, but with the reconstruction initialized assuming a uniform layer of proton spins on the surface.

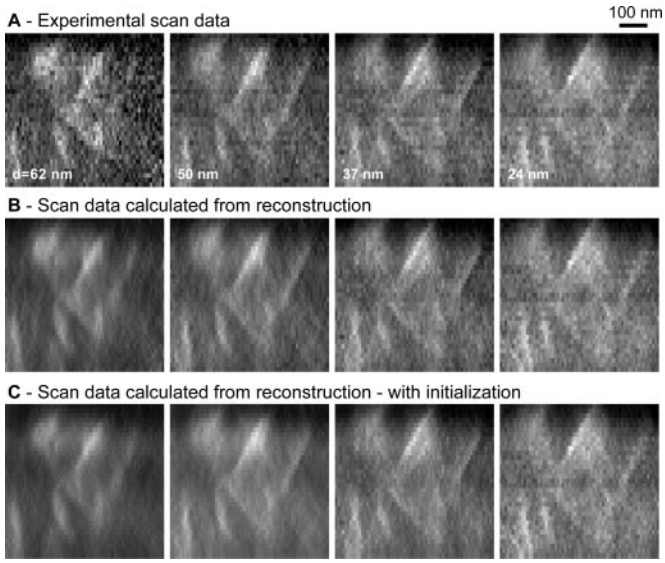

Fig. S7. Comparison of experimental scan data to the data predicted by the reconstruction. (*A*) Experimental data corresponding to Fig. 4 in the main text. Labels indicate the distances between magnetic tip and the virus particles. (*B*) Data predicted from the reconstructed spin density where initial guess in the Landweber reconstruction was zero spin density. (*C*) Same as *B*, but with the reconstruction initialized assuming a uniform layer of proton spins on the surface.